Dynamic impact behavior and deformation mechanisms of Cr$_{26}$Mn$_{20}$Fe$_{20}$Co$_{20}$Ni$_{14}$ high-entropy alloy

Wei Jiang [a], Xuzhou Gao [a], Yazhou Guo [b], Xiang Chen [a,*], Yonghao Zhao [a,**]

[a] Nano and Heterogeneous Materials Center, School of Materials Science and Engineering, Nanjing University of Science and Technology, Nanjing, 210094, China
[b] School of Aeronautics, Northwestern Polytechnical University, Xi'an, 710072, China

ABSTRACT

In this work, the dynamic impact behavior and linked deformation mechanisms of a Cr$_{26}$Mn$_{20}$Fe$_{20}$Co$_{20}$Ni$_{14}$ high-entropy alloy (HEA) with face-centered cubic structure were systematically explored. The HEA displays uniform plastic deformation without any adiabatic shear bands at a strain rate range from 1000 to 3000 s^{-1}. Moreover, the yield strength exhibits a pronounced strain rate dependence, increasing by 28% from 282 MPa at 1000 s^{-1} to 360 MPa at 3000 s^{-1}. The strain hardening exponent, strain rate sensitivity and temperature rise were calculated to be 0.899–0.95, 0.076 and 64.7 K, respectively, indicative of high strain and strain-rate hardening capabilities and strong resistance to thermal softening induced adiabatic shear localization. Detailed microstructural analyses decipher a transition of deformation mechanism from dislocation slip at 1000 s^{-1} to stacking faults (SFs) at 2000 s^{-1} and further to twinning at 3000 s^{-1}, respectively. The strengthening mechanisms are delineated as manifold interactions between glide dislocations and SFs, SFs and SFs (i.e. the Lomer-Cottrell locks), and SFs and twins. Our work provides a comprehensive understanding on the dynamic impact behavior, deformation and strengthening mechanisms of Cr$_{26}$Mn$_{20}$Fe$_{20}$Co$_{20}$Ni$_{14}$ high-entropy alloy.

1. Introduction

In 2004, a completely new design concept of high-entropy alloys (HEAs), also known as multi-component alloys, was coined by *Ye* et al. and *Cantor* et al., respectively. In contrast to conventional wisdom with only one dominant component in the alloy, HEAs are composed of more than four dominant elements with near equal atomic percentages [1–3]. The huge compositional space gives rise to enormous opportunities in seeking materials with unprecedented property profiles [4–10]. So far, single-phase Cantor family alloys with face-centered cubic (FCC) structure, including equiatomic CrMnFeCoNi and CrFeCoNi HEAs are the most thoroughly investigated, as they display excellent strength and toughness at room temperature [11,12]. Besides, the dual-phase Cr$_{10}$Mn$_x$Fe$_{80-x}$Co$_{10}$ HEAs with low stacking fault energy (SFE) possess an unparalleled synergy between strength and ductility [13]. These are mainly ascribed to the joint activation of multiple deformation mechanisms such as twinning and phase transformation, enabling HEAs to be dynamically strengthened by the twinning-induced-plasticity (TWIP) and transformation-induced plasticity (TRIP) effects and even their combined effects [14,15]. Furthermore, the low SFE reduces the critical resolved shear stress for twinning and phase transformations, thereby boosting the TWIP and TRIP effects.

A plethora of investigations have pointed out that the dominated deformation mechanisms of HEAs are intimately dependent upon not only the intrinsic parameters of materials (e.g. SFE) but also deformation conditions (such as strain, temperature and strain rate) [16–19]. A seminal work of CrMnFeCoNi HEA (25 mJm^{-2}) has achieved excellent strength-ductility synergy with continuous strain hardening at cryogenic temperature (77 K), which was primarily attributed to the activation of deformation twins at cryogenic temperature [6]. Later on, careful microstructural characterization show that twins were initiated much earlier (true strain, 7.4%) during tensile deformation of CrMnFeCoNi HEAs at 77 K, compared to twins rarely detected at the late stage (true strain, 25%) at room temperature [11,20]. More recently, *Naeem* et al. revealed that the activation tensile strain for stacking faults (SFs) formation follows a monotonous decrease with decreasing temperature for the CrMnFeCoNi HEA, decreasing from ~37% at 295 K to 22% at 140 K and then to 16% at 15 K, respectively [21]. These low temperature results of HEAs are strongly indicative of their untapped potential of utilization under extreme environments.
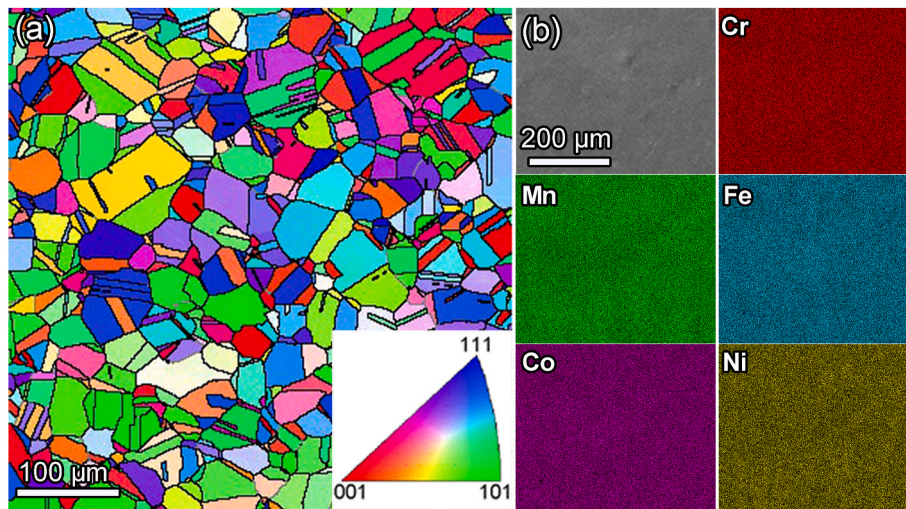
Fig. 1. (a) A typical EBSD mapping of the annealed $Cr_{26}Mn_{20}Fe_{20}Co_{20}Ni_{14}$ HEA before the Hopkinson test (The inset is the Inverse Pole Figure color code). (b) SEM-EDS maps of the alloy and the distributions of alloying elements (Cr, Mn, Fe, Co and Ni) in the HEA. (For interpretation of the references to color in this figure legend, the reader is referred to the Web version of this article.)

According to Zener-Hollomon equation, high strain rate (HSR) is deemed favorable for the activation of twinning and phase transitions, analogous to the effect of cryogenic temperature [22]. For instance, *Yang* et al. exemplified a mechanism conversion from dislocation slip to twinning with increasing strain rate from $3 \times 10^3 \text{ s}^{-1}$ to $9 \times 10^3 \text{ s}^{-1}$ in the CrMnFeCoNi alloy [23]. *Wang* et al. revealed a superior strength-ductility synergy under HSR loading of $Al_{0.6}CrFeCoNi$ HEAs, thanks to the activation of deformation twins and abundant dislocations [24]. It was further interpreted that HSR favors rapid dislocation accumulation and thus the severely concentrated stress, which consequently provides valid nucleation sites for deformation twins [24]. Although a myriad of deformation mechanisms were anticipated in the HSR regime [25], the onset and sequences of respective mechanisms and their interactions remain largely unexplored, even for the CrMnFeCoNi family alloys.

In the present work, a non-equiatomic $Cr_{26}Mn_{20}Fe_{20}Co_{20}Ni_{14}$ HEA with low SFE was chosen for the HSR investigation. Our early work demonstrated that the SFE of the $Cr_{26}Mn_{20}Fe_{20}Co_{20}Ni_{14}$ HEA was 24 mJm^{-2} [26]. Our previous results have revealed that this HEA possessed enhanced strain hardening ability and higher ductility (73%) [26], compared with those of other CrMnFeCoNi family alloys [5,27–29]. Our research focus is therefore to assess its capability to withstand dynamic loading and appraise the detailed deformation mechanisms.

2. Experiments

The $Cr_{26}Mn_{20}Fe_{20}Co_{20}Ni_{14}$ (actual atomic percent) alloy ingot was prepared by melting commercially pure elements (Cr, Mn, Fe: 99.5–99.6 wt%; Co, Ni: 99.9 wt%) in a boron nitride (BN) crucible in a medium frequency vacuum induction melting furnace. The BN crucible containing the mixture of raw materials was preheated at 873 K by 1 h for removal of water vapor. Prior to the melting process, the furnace chamber was evacuated to 0.01 Pa with the protection of high purity argon gas to 0.06 MPa. Once reaching the liquid state, it was held at 1823 K for 15 min and then poured into a MgO crucible coated by ZrO_2. The temperature in the furnace was monitored by an IRTM-2CK infrared pyrometer with a minimal error of ± 2 K. The alloys were re-melted twice in an effort to improve the chemical homogeneity. Hot-forged at 1273 K and subsequent annealing at 1273 K for 8 h were performed on the as-cast $Cr_{26}Mn_{20}Fe_{20}Co_{20}Ni_{14}$ ingot to achieve recrystallized equiaxed grains.

As-annealed HEA ingot was cut into samples with dimensions of $5 \times 5 \times 5 \text{ mm}^3$ for HSR uni-axial compression. The samples were ground and

the surfaces parallel to the impact direction were then mechanically polished to obtain smooth and mirror-like surface finish in order to easily distinguish the slip traces. HSR uni-axial dynamic loading was performed using a Split Hopkinson Pressure Bar (SHPB) system at strain rates ranging from 1000 to 3000 s^{-1}. The tests were repeated three times for each strain rate. The bars with a diameter of 12.7 mm and a length of 150 mm were made by maraging steel with elastic modulus of 190 GPa. The details of the working principles and cautions of the SHPB technique can be obtained in Refs. [30,31].

Scanning electron microscopy (SEM) equipped with energy-dispersive spectrometer (EDS), electron back-scattered diffraction (EBSD), transmission electron microscopy (TEM) and high-resolution transmission electron microscopy (HRTEM) analyses were carried out to study the microstructures and compositions of the $Cr_{26}Mn_{20}Fe_{20}Co_{20}Ni_{14}$ HEA. Both EBSD and EDS specimens were mechanically polished and subsequently electropolished for mirror-like surface finish. A Buehler ElectroMet 4 polisher and an electrolyte containing 10 vol% perchloric acid and 90 vol% acetic acid have been used for the experiment. Under the applied voltage of 20 V, a shiny mirror-like surface can be achieved for the sample within 30 s by the electropolishing process. TEM and HRTEM observations were performed by an FEI-Tecnai G^2 20 S-TWIN microscope at 200 kV and a Titan G^2 60–300 microscope at 300 kV, respectively. The TEM specimens were prepared by grinding the specimen down to 60 μm thickness and then punching into disks with a diameter of 3 mm. The disks were electro-polished in a twin jet electron-polishing system containing an aqueous electrolyte of 25% perchloric acid and 75% acetic acid at 20 °C.

3. Results

3.1. Initial microstructures and distributions of compositions

As shown in Fig. 1a, the as-annealed $Cr_{26}Mn_{20}Fe_{20}Co_{20}Ni_{14}$ HEA sample has equiaxed grains with a mean grain size of 33 μm. Annealing twins are discernible in the grain interior. Besides, the EBSD orientation map with the inset of inverse pole figure in Fig. 1a, indicates that the grains are randomly orientated. SEM-EDS maps (Fig. 1b) reveal that all five elements (Cr, Mn, Fe, Co, Ni) are homogeneously distributed within the area of interest ($500 \times 400 \text{ μm}^2$). Grain boundary segregation or second phase particles are not visible in present HEA, which is different from the Mn segregation observed in FeMn- and FeMnNi-based alloys [32–34].
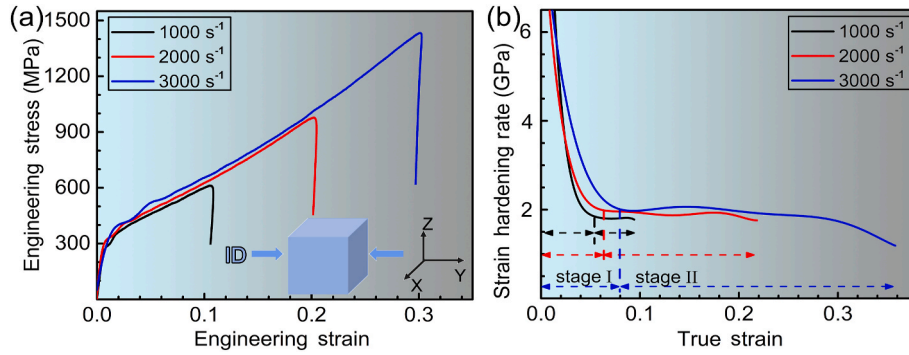
Fig. 2. Hopkinson impact properties of $Cr_{26}Mn_{20}Fe_{20}Co_{20}Ni_{14}$ HEA. (a) Engineering stress-strain curves at 1000, 2000 and 3000 s^{-1}. Inset shows that the impact direction (ID) is along the Y axis. (b) Strain hardening rate as a function of true strain. The dashed lines indicate two well-defined stages under each strain rate.

Table 1
A list of Hopkinson impact properties, temperature rise ΔT, dislocation density ρ and volume fraction of twin boundary (TB Vol. %) of $Cr_{26}Mn_{20}Fe_{20}Co_{20}Ni_{14}$ HEA at different strain rate.

$\dot{\varepsilon}$ (s^{-1})	σ_y (MPa)	$\sigma_{\varepsilon=0.1}$ (MPa)	ε_{total} (%)	ΔT (K)	ρ ($\times 10^{14}$ m^{-2})	TB Vol. (%)
1000	282	533	0.114	13	0.9	29
2000	300	553	0.226	33	2.17	38
3000	360	581	0.358	65	6.41	52

3.2. Hopkinson impact properties

Fig. 2a shows the Hopkinson impact engineering stress-strain curves of the $Cr_{26}Mn_{20}Fe_{20}Co_{20}Ni_{14}$ HEA deformed at room temperature over a strain rate range from 1000 to 3000 s^{-1}. Continuous absorption of the impact energy is manifest by the increased dynamic compressive stress with the increasing strain. It is worth noting that the drop of flow stress

in the curves suggest the end of the compression loading pulse on the Hopkinson bar, rather than the failure of samples. The yield strength (σ_y) increases by 28% from 282 MPa at 1000 s^{-1} to 360 MPa at 3000 s^{-1} (Table 1), indicating enhanced strain rate hardening ability with increasing strain rate. Such a trend is a typical feature of the alloys with low SFEs [35–37], such as 304L stainless steel, nitrogen-alloyed austenitic steel [37] and Cu-x(wt.%) Al (x = 0.2, 2 and 6) alloys [38]. With the strain rate increasing to the HSR regime (>1000 s^{-1}), the prefect dislocations pinned by the phonon drag effect could not match the imposed HSR, thereby the higher driving stress is applied to induce massive partial dislocations in the samples, especially for the alloys with low SFEs.

The strain hardening rate Θ ($\Theta = \partial\sigma_t/\partial\varepsilon_t$, where σ_t denotes the true stress and ε_t is the true strain) curves is shown in Fig. 2b and exhibit two distinct stages at all measured strain rates. The Θ keeps positive values throughout the compression impact for each strain rate, in contrast to the negative values of Θ in stainless steels due to shear bands caused by local thermal softening [39,40]. In stage I, the significant drop of Θ
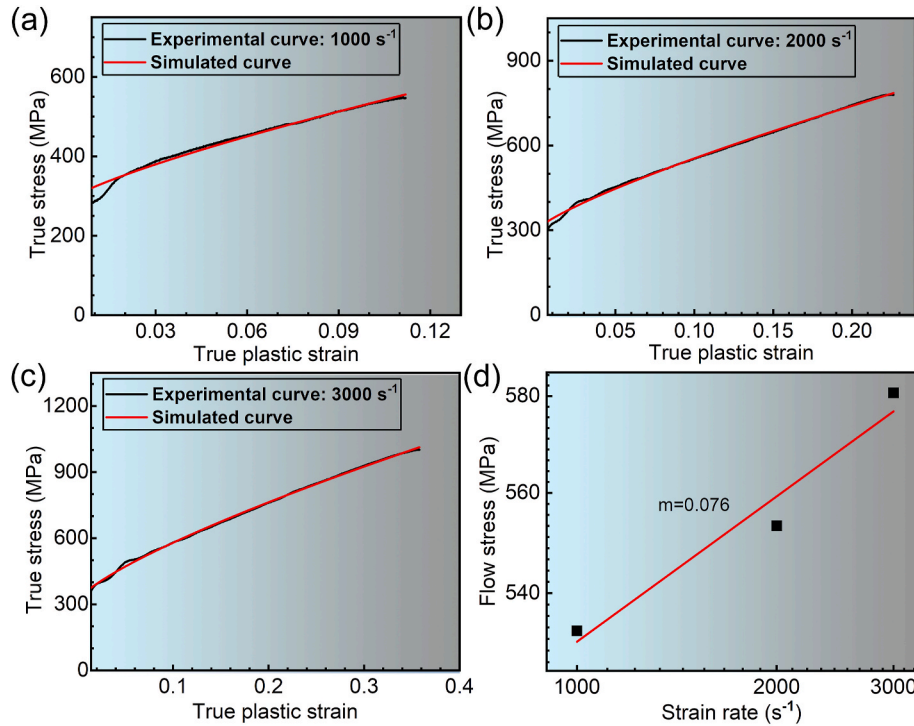
Fig. 3. Experimental true stress-strain curves of $Cr_{26}Mn_{20}Fe_{20}Co_{20}Ni_{14}$ HEA and simulated curves by Ludwick ($\sigma_t = \sigma_y + K\varepsilon_t^n$) equations at (a) 1000 s^{-1}, (b) 2000 s^{-1} and (c) 3000 s^{-1}. (d) Strain rate sensitivity m obtained by constant strain rate method, in which the flow stress is a function of strain rate on a double logarithmic scale.

Table 2
Lists of the values of the strain hardening exponent, n, and strengthening coefficient K simulated by the Ludwick ($\sigma_t = \sigma_y + K\varepsilon_t^n$) equation.

$\dot{\varepsilon}$ (s^{-1})	σ_y (MPa)	K (MPa)	n
1000	282	1687	0.83
2000	300	2009	0.899
3000	360	2218	0.95

corresponds to the conventional elasto-plastic conversion region [41]. In addition, the strain range of the stage I broadens with the increasing strain rate, attributing to the hysteretic slip of dislocations at HSR [42]. There exists a plateau in stage II, which is different from the monotonous decrease of conventional materials with high SFEs [43]. Note that the oscillations in the Θ curves stem from the nature of elastic wave propagation in cylinder bars [44].

Strain hardening exponent n is determined by Ludwick ($\sigma_t = \sigma_y + K\varepsilon_t^n$) equation (where K is the strength coefficient) in an effort to evaluate the extent of strain hardening. Apparently, the simulated curves by

Ludwick equations coincide with the experimental data for each strain rate (Fig. 3). The simulated n increases from 0.899 to 0.95 with strain rate rising from 1000 to 3000 s^{-1} (see Table 2). Besides, the strain rate sensitivity m is a critical parameter to assess the rate-dependent deformation mechanisms. The determination of m values is based on the constant strain rate method [30]. Then m can be described as:

$$m = \frac{\partial ln\sigma}{\partial ln\dot{\varepsilon}} \tag{1}$$

where σ is the flow stress corresponding to a true strain of 0.1, as shown in Table 1. The average m value is calculated to be 0.076, as shown in Fig. 3d.

3.3. Postmortem microstructure results

Fig. 4 shows the SEM micrographs taken from the surface on the YZ-plane (inset in Fig. 2a) of the Cr$_{26}$Mn$_{20}$Fe$_{20}$Co$_{20}$Ni$_{14}$ samples after loading. The rough and granular morphology are observed in Fig. 4a-c,
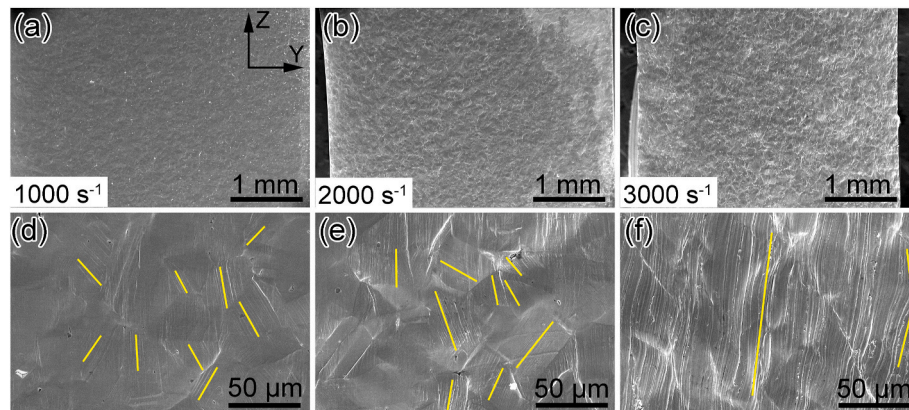
Fig. 4. SEM images of the surface on the YZ-plane showing post-loading surface of the Cr$_{26}$Mn$_{20}$Fe$_{20}$Co$_{20}$Ni$_{14}$ HEA at 1000 (a), 2000 (b) and 3000 s^{-1} (c) respectively. (d), (e) and (f) High magnification images to show detailed slip traces (marked by yellow lines) in (a), (b) and (c) respectively. (For interpretation of the references to color in this figure legend, the reader is referred to the Web version of this article.)
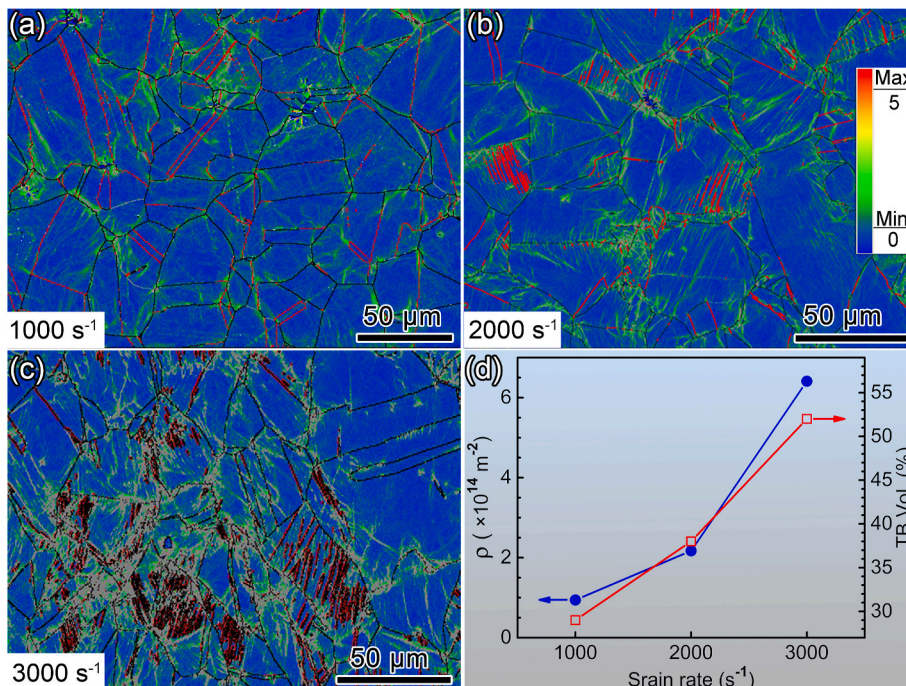
Fig. 5. (a–c) EBSD local misorientation maps of the Cr$_{26}$Mn$_{20}$Fe$_{20}$Co$_{20}$Ni$_{14}$ HEA subjected to Hopkinson impact testing at 1000 (a), 2000 (b) and 3000 s^{-1} (c), respectively. (TBs are depicted by red lines) (d) Variations of dislocation density (ρ) and volume fraction of twin boundary (TB Vol.) of the samples subjected to Hopkinson impact testing at 1000, 2000 and 3000 s^{-1}, respectively. (For interpretation of the references to color in this figure legend, the reader is referred to the Web version of this article.)
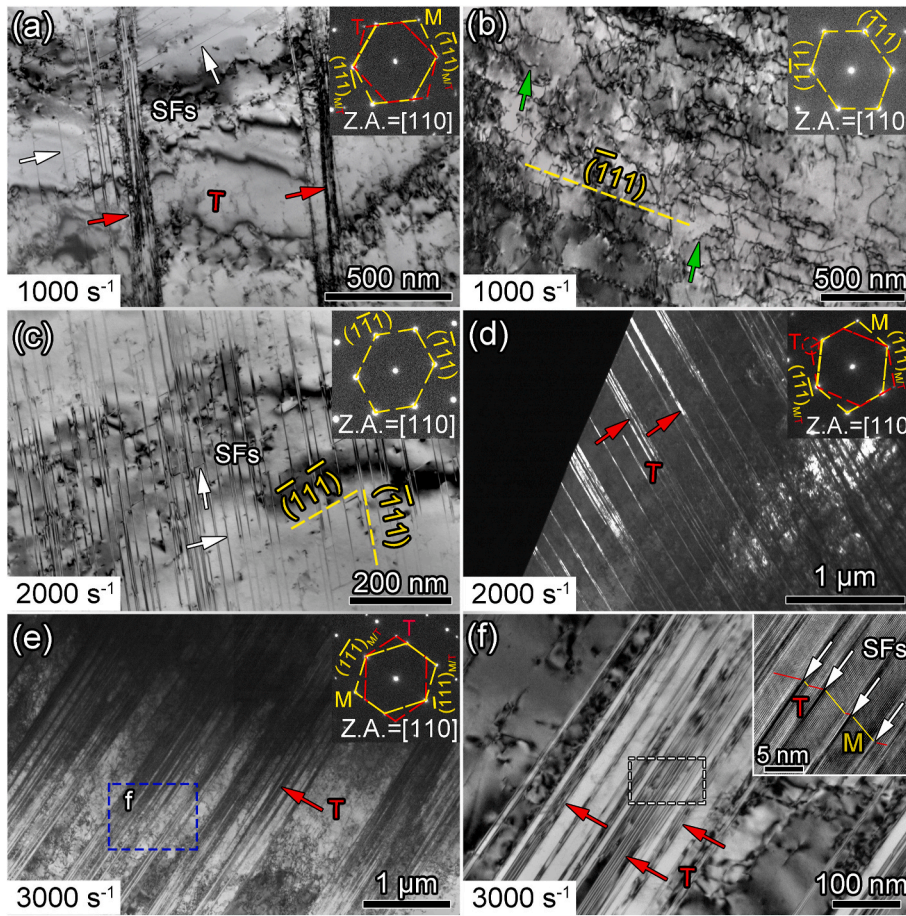
Fig. 6. TEM images of the $Cr_{26}Mn_{20}Fe_{20}Co_{20}Ni_{14}$ HEA impacted at different strain rate. (a) Some stacking faults (SFs) and twins (T) in the sample impacted at 1000 s^{-1}. (b) Typical dislocation configurations and trace of edge-on ($\bar{1}11$) slip planes in the sample impacted at 1000 s^{-1}. (c) Bright field image showing massive SFs on {111} planes in the sample impacted at 2000 s^{-1}. (d) Dark field image with insets of SAED pattern of the matrix (M) and T, showing twins and dislocations within twin lamellae. Diffraction spot used for dark field image was marked by one red circle. (e) Typical dislocation structures and deformation twins in the sample impacted at 3000 s^{-1}. (f) Enlarged image of nano-twin bundles (indicated by red arrows). Inset is an HRTEM image showing nano-twin bundles in detail. (For interpretation of the references to color in this figure legend, the reader is referred to the Web version of this article.)

and the surface appears to be rougher at higher strain rate. In addition, the evidence of shear bands and microcracks are not captured in all the samples, indicating a continuous hardening process. The slip traces (marked by yellow lines) increase and distribute more homogeneously within grains (Fig. 4d-f). This result is correlated with the increasing final strain: 0.114 at 1000 s^{-1} to 0.226 at 2000 s^{-1}, and up to 0.358 at 3000 s^{-1}.

EBSD characterizations were carried out in order to quantitatively characterize the microstructural changes. Fig. 5a-c show the local misorientation map at 1000, 2000 and 3000 s^{-1} respectively. It is seen that massive deformation twins (the TBs were depicted by red lines) are

activated in the grain interiors of all the samples. The volume fraction of the TBs increases from 29% at 1000 s^{-1} to 52% at 3000 s^{-1} (Fig. 5d), indicating deformation twinning is the dominating deformation mechanism under Hopkinson impact at 3000 s^{-1}. In addition, the misorientation increases with the raising strain rate, indicating a higher density of dislocations accumulated at higher strain rate. The dislocation density can be calculated according to the equation [45,46]:

$$\rho = \frac{2\theta_{KAM}}{xb} \tag{2}$$

where ρ is the dislocation density, θ_{KAM} is the kernel average
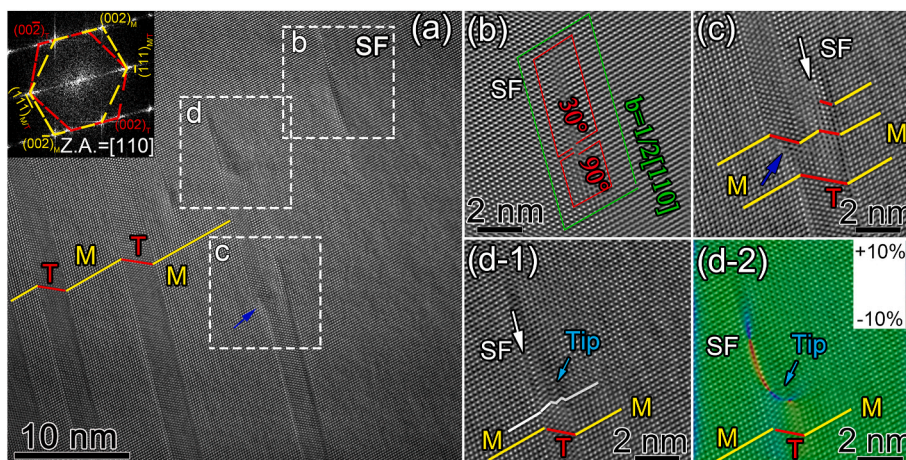
Fig. 7. HRTEM images of the $Cr_{26}Mn_{20}Fe_{20}Co_{20}Ni_{14}$ HEA with a strain rate of 2000 s^{-1}. (a) Deformation twins and SF. The inset is the entire Fourier transformation (FFT) pattern. (b) The magnified image from the region labeled "b" in (a), showing the formation of SF by the dissociation of a full dislocation 1/2<110> to two 1/6<112> partial dislocations. (c) The magnified image from the region labeled "c", showing the step on TB (marked by blue arrow). (d-1) The magnified image from the region labeled "d", showing the front of twin tip (marked by cyan arrow). (d-2) Image of geometric phase analysis (GPA), showing a high strain field along the residual SF at the front of twin tip. (For interpretation of the references to color in this figure legend, the reader is referred to the Web version of this article.)
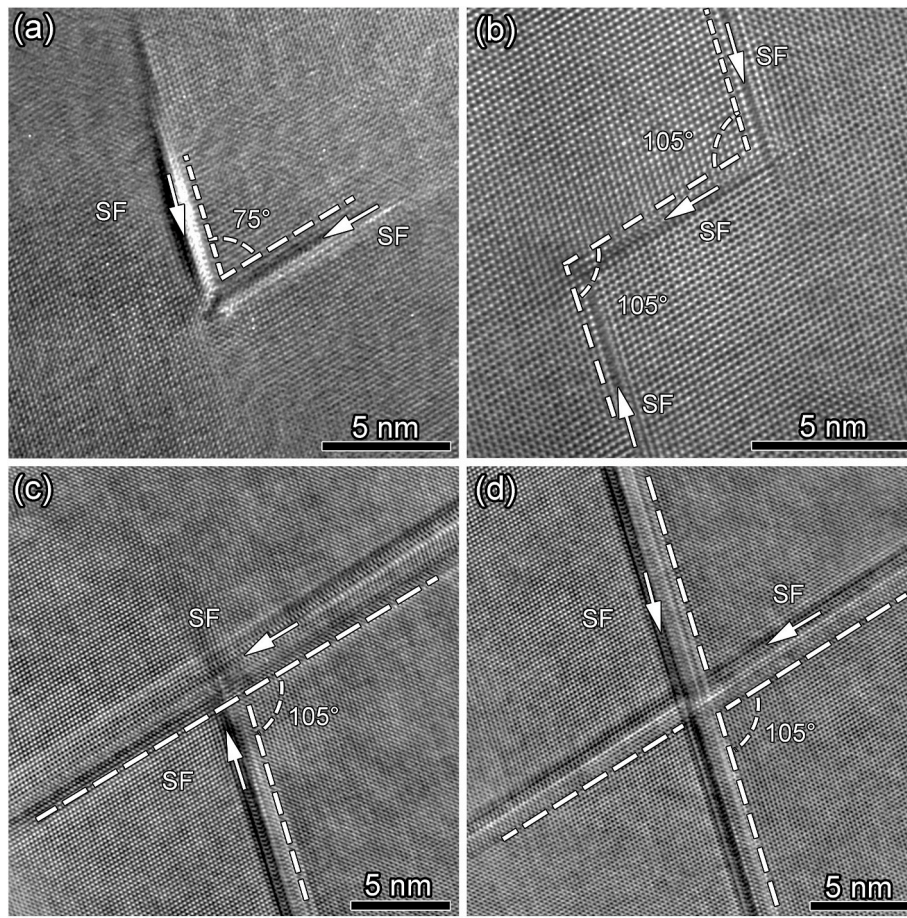
Fig. 8. HRTEM images showing four types SF configuration in the $Cr_{26}Mn_{20}Fe_{20}Co_{20}Ni_{14}$ HEA under strain rate of 2000 s^{-1}. (a) V-shaped SF configuration with acute angle of 75°. (b) V-shaped SF configurations with obtuse angle of 105°. (c) T-shaped SF configuration with angle of 105°. (d) X-shaped SF configuration with angle of 105°.

misorientation, x (300 nm) is the unit length, twice that of the step size used in EBSD acquisition, b (0.253 nm) is the magnitude of Burgers vector. As shown in Fig. 5d, the dislocation density increases substantially from 9×10^{13} m^{-2} at 1000 s^{-1} to 2.17×10^{14} m^{-2} at 2000 s^{-1}, and further to 6.41×10^{14} m^{-2} at 3000 s^{-1}.

As shown in Fig. 6, TEM observations of post-mortem specimens were performed to further reveal the deformation mechanisms of the $Cr_{26}Mn_{20}Fe_{20}Co_{20}Ni_{14}$ HEA subjected to Hopkinson impact testing. As shown in Fig. 6a and b, the [110] zone axis (Z.A.) bright-field (BF) micrographs of samples tested at 1000 s^{-1} show that {111} type planar slip is activated, forming continuous slip traces and a high density of dislocations. In addition, some SFs (marked by white arrows) and nano-twin lamellae (marked by red arrows) are formed in the grain interior. Moreover, bowed dislocations (marked by green arrows) are frequently observed in Fig. 6b, which can be explained by the Labusch-type solid solution strengthening in concentrated solid solutions [29]. The appearance of planar slip in (111) planes is due to the low SFE of this HEA, as previously confirmed by exact muff-tin orbital method (3.5 mJm^{-2}) [47] and HRTEM measurement (24 mJm^{-2}) [26]. As the strain rate increases to 2000 s^{-1}, the density of SFs and twins increase significantly. As shown in Fig. 6c, massive SFs are activated on {111} slip systems in one grain. Fig. 6d shows profuse nano-scale twin lamellae in one grain and high density of dislocations accumulated within the twin and matrix as well. The uniform distribution of dislocations in the present HEA is distinctly different from dislocation cells observed in FCC materials with medium to high SFEs [48]. With the strain rate increasing to 3000 s^{-1}, twinning becomes the dominating deformation mechanism. A high density of twins with thicknesses of 10–50 nm are formed in the

grain (Fig. 6e and f). Apart from the twins, we also observe the SFs and dislocation structure.

The HRTEM images (Fig. 7a and b) were taken to reveal the generation of SFs and twins and their interactions. First, the formation of SF is by the dissociation of a full dislocation 1/2<110> to two 1/6<112> partial dislocations, as shown in Fig. 7b. In addition, residual SFs are found along the TB and at the front of twin tip (Figures 7c and **d-1**). Furthermore, the geometric phase analysis (GPA) of Figs. 7d-1, quantifies noticeable strain fields along the residual SF within TB and at the front of twin tip (Figs. 7d-2), hinting that stronger forces are necessitated for the SFs and twins on impeding moving dislocations. Moreover, the interaction of two SFs on conjugate {111} planes form four types of SF configurations (Fig. 8): V-shaped with angles of 75° and 105° (Fig. 8a and b), T-shaped (Fig. 8c) and X-shaped SFs (Fig. 8d).

4. Discussion

4.1. Resistance to thermal softening

The current HEA exhibits a strong resistance to adiabatic shear localization, which is considered as an imperative failure mechanism under HSR deformation. In particular, the temperature rise induced thermal softening is always taken into consideration when analyzing adiabatic shear localization. In our case, the temperature rise ΔT is calculated by the work imposed upon the material during deformation as follows [49]:
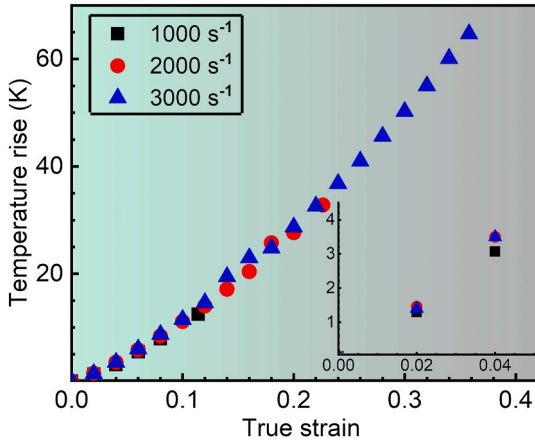
Fig. 9. Temperature rise ΔT versus true strain ε at different strain rates $\dot{\varepsilon}$. The inset is enlargement of the true strain range of 0–0.05.

$$\Delta T = \frac{\beta}{\rho C_p} \int_0^\varepsilon \sigma d\gamma \tag{3}$$

where β is the ratio of plastic work converted into heat, ρ is the density and C_p represents the specific heat capacity. The density of the current HEA was measured to be 7.76×10^3 kg/m^3 using the water immersion method. The C_p of the present HEA is about 0.45414 kJ/(kg· K) by utilizing a weight averaging method $C_p = \omega_i \sum_{i=1}^{5} C_{pi}$ (ω_i and C_{pi} are the weight percent and specific heat capacity for each element of the alloy, respectively) [50]. As shown in Fig. 9, increasing strain and strain rate both bring about temperature rise. At higher strain rate, the cooling time is insufficient, inevitably leading to higher temperature rise (at the same strain). The highest temperature rise ΔT is about 64.7 K at the maximum strain of 0.358 under 3000 s^{-1}, which is much less than its recrystallization temperature (0.4 T_m, T_m is the melting temperature being around 1600 K), bypassing the thermal softening induced adiabatic shear localization.

4.2. Strain rate hardening

It is notable that the m value (0.076) of our Cr$_{26}$Mn$_{20}$Fe$_{20}$Co$_{20}$Ni$_{14}$ HEA is larger than that of the equiatomic CrMnFeCoNi HEA (0.028) [51] and that of the equiatomic CrFeCoNi HEA (0.048) [29]. Especially, this value is one order of magnitude higher than traditional FCC materials, such as pure Ni (0.0028) and pure Cu (0.006) [52,53]. The high m is

presumably due to the accumulation of dislocations induced by massive SFs and deformation twins (Fig. 5d), as the value of m is intimately rated to the microstructural changes [51,54,55]. It is widely accepted that the activation volume can be used to evaluate the strain rate hardening ability, together with the strain rate sensitivity. The activation volume can be estimated as a function of the inverse of m as follows:

$$V^* = \sqrt{3}k_B T \frac{\partial ln\dot{\varepsilon}}{\partial \sigma} = \frac{\sqrt{3}k_B T}{\partial \sigma} \frac{\partial ln\sigma}{m} \tag{4}$$

where k_B and T are Boltzmann constant and temperature, respectively. Here, the activation volume V^* is given in units of b^3. The calculated V^* of the Cr$_{26}$Mn$_{20}$Fe$_{20}$Co$_{20}$Ni$_{14}$ HEA is about 11 b^3, smaller than that of CrMnFeCoNi HEA (76.8 b^3) [29]. Compared with traditional FCC metals, such as Cu (200–2000 b^3) and Cu–Zn alloy (200–400 b^3), this value is much smaller [56]. It is speculated that the tiny activation volume of the Cr$_{26}$Mn$_{20}$Fe$_{20}$Co$_{20}$Ni$_{14}$ HEA may be attributed to the high friction stress generated from the short-range order and the pining effect by the solid solution in HEAs [57–59]. Moreover, high density deformation twins and dislocation-twin interactions contribute to the low activation volume V^* of the Cr$_{26}$Mn$_{20}$Fe$_{20}$Co$_{20}$Ni$_{14}$ HEA, which is consistent with the reported activation volume value for dislocation-twin interactions (1–100 b^3) [29].

4.3. Strain hardening

The remarkable density of twins, SFs and dislocations provide sufficient strain hardening ability for the Cr$_{26}$Mn$_{20}$Fe$_{20}$Co$_{20}$Ni$_{14}$ HEA subjected to Hopkinson impact tests. The underlying mechanisms will be discussed in the following three aspects.

4.3.1. Dislocation strengthening

To evaluate the extent of strain hardening, Ludwick equation is utilized to deduce the exponent n. As shown in Fig. 3 and Table 2, the values of n reach as high as 0.8–0.95 and increase with the rise of the strain rate. The high n is indicative of strong strain hardening ability associated with dislocation storage capacity and superior capability to withstand the high impact energy. First, the low SFE renders cross-slip and climb of dislocations difficult, thus facilitating dislocation accumulation in the current HEA. Second, the multi-principal element design significantly elevates the dislocation storage capacity due to the unique atomic structure. A recent in-situ TEM investigation revealed that the strong drag effect caused by the solute atoms leads to slip of perfect and partial dislocations with tremendously low velocity [60]. In addition, the planar slip bands (Fig. 6b) serve as strong barriers for dislocation motion, enabling strong strain hardening [60].
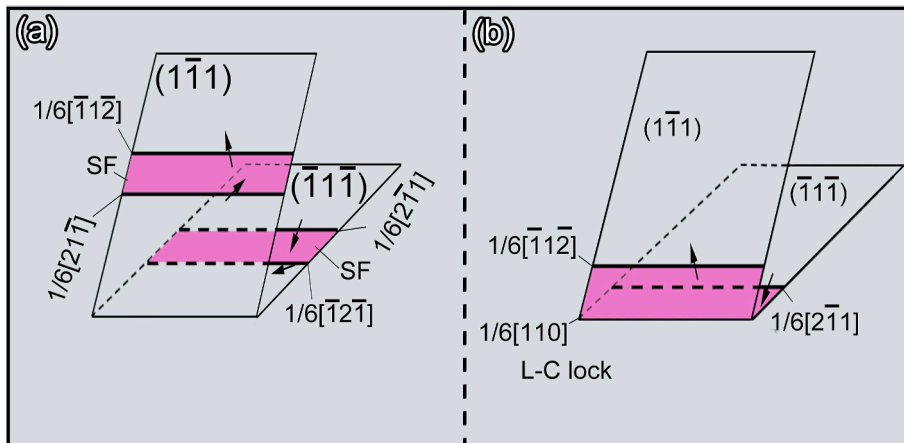
Fig. 10. Illustration of the formation of a Lomer-Cottrell lock by the reaction of two SFs on conjugate {111} planes.
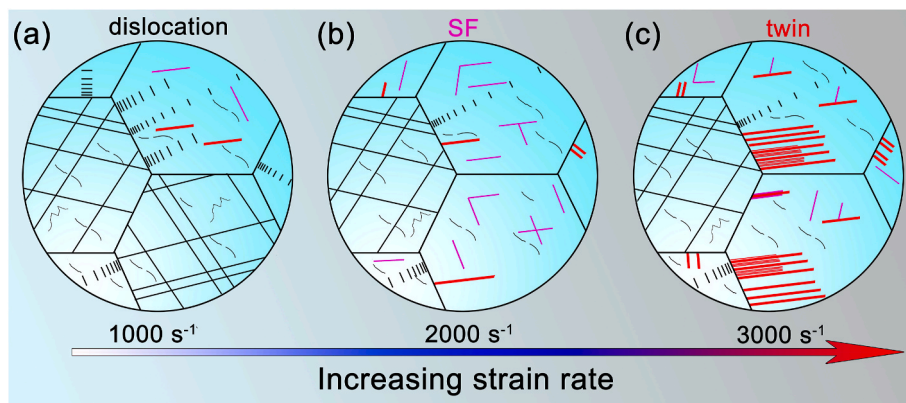
Fig. 11. Schematic illustration of the deformation mechanisms of the $Cr_{26}Mn_{20}Fe_{20}Co_{20}Ni_{14}$ HEA with increasing stain rate. (a) Dislocation slip. (b) SF dominated mechanism. (c) Nano-twinning dominated mechanism.

4.3.2. SFs strengthening

It was established that the SFs could act as obstacles to effectively impede the motion of dislocations [61] and the interaction between glide dislocations and SFs could bring about continuous strain hardening [62]. In the present work, it is reasonable to assume that accumulated formation of V-, T- and X-shaped SFs by SF reaction provides remarkable strain hardening in the $Cr_{26}Mn_{20}Fe_{20}Co_{20}Ni_{14}$ HEA. As illustrated in Fig. 10a and b, the reaction between two leading partial dislocations results in a sessile stair-rod dislocation by:

$$\frac{a}{6}<2-11>+\frac{a}{6}<-12-1>\rightarrow\frac{a}{6}<110> \quad (5)$$

Such a configuration containing a stair-rod dislocation on a {100} plane is known as the Lomer-Cottrell lock [63]. The networks of Lomer-Cottrell locks could act as Frank-Read sources for dislocation multiplication [16], leading to strengthening of the present HEA. Besides, the stair-rod dipole forming at the intersection of SFs induces high stress field to hinder the moving dislocations, wherein the attractive force can reach as high as 10^9 N/m^2 [64,65].

4.3.3. Twinning strengthening

Twinning has been proved to be an imperative strengthening mechanism in HEAs with low SFE [5,17]. *Zhang* et al. revealed that deformation twins as well as interactions between dislocations and TBs noticeably affect the deformation process of the CrFeCoNi HEA and contribute to the enhanced mechanical properties under dynamic loading [16]. In the $Cr_{26}Mn_{20}Fe_{20}Co_{20}Ni_{14}$ HEA, massive deformation twins (52% in volume fraction at 3000 s^{-1}) are observed, thereby substantially contributing to the strain hardening effect. Upon deformation, deformation twins instantly generate additional boundaries and induce back stress, which decreases the dislocation mean free path and increases the dislocation storage capacity [62,66,67]. This can be reflected by abundant dislocations distributed within the twin and matrix at high strain rates (see Fig. 6). Besides, plenty of nano-twin bundles with thinner twin lamellae (Fig. 6f) trigger stronger external stress for dislocations across TBs and thus sufficiently inhibit the process of dislocation annihilation [68].

Above all, the stages of microstructural changes and associated deformation mechanisms of the $Cr_{26}Mn_{20}Fe_{20}Co_{20}Ni_{14}$ HEA at HSR are schematically illustrated in Fig. 11. The dislocation glide governs the deformation process at a low strain rate of 1000 s^{-1}. With increasing strain rate to 2000 s^{-1}, SFs and nano-twinning become the dominating deformation mechanisms. Four unique SFs configurations are formed by the intersection of the SFs on two {111}<11$\bar{2}$> slip systems. The highest strain rate of 3000 s^{-1} results in high dislocation density and nano-twin bundles. The SFs interaction containing sessile Lomer-Cottrell lock and numerous deformation twinning enable sustained hardening ability and superior dynamic properties, significantly getting rid of thermal softening and adiabatic shear localization in the $Cr_{26}Mn_{20}Fe_{20}Co_{20}Ni_{14}$ HEA.

5. Conclusions

In this work, Hopkinson impact tests were performed to investigate the dynamic properties of a coarse grained $Cr_{26}Mn_{20}Fe_{20}Co_{20}Ni_{14}$ HEA with a SFE of 24 mJm^{-2}. The post-deformed samples were examined to elucidate the deformation and strengthening mechanisms encountering high strain rates. Several conclusions are drawn as follows:

1. The dynamic impact properties present strong strain rate dependence, e.g. the yield strength, σ_y, increases by 28% from 282 MPa at 1000 s^{-1} to 360 MPa at 3000 s^{-1}. The strain hardening exponent n determined by the Ludwick equation increase from 0.899 to 0.95 with the increase of strain rate from 1000 to 3000 s^{-1}.
2. The temperature rise ΔT is estimated to be 64.7 K, far below its recrystallization temperature, avoiding the thermal softening induced adiabatic shear localization. The high strain rate sensitivity m (0.076) and low activation volume V^* (11 b^3) indicate high strain and strain-rate hardening capabilities for the current HEA.
3. Microstructural analyses at different strain rates decipher a transition of deformation mechanisms from dislocation slip at 1000 s^{-1} to generation of SFs at 2000 s^{-1} and twinning at 3000 s^{-1}, respectively. The interactions of glide dislocations with SFs, the SFs-SFs reactions (i.e. the Lomer-Cottrell locks) and SFs-twins are delineated as the prominent strengthening mechanisms under dynamic loading.

CRediT authorship contribution statement

Wei Jiang: Data curation, Visualization, Writing – original draft. **Xuzhou Gao:** Investigation. **Yazhou Guo:** Investigation, Validation. **Xiang Chen:** Writing – review & editing, Funding acquisition. **Yonghao Zhao:** Conceptualization, Supervision, Writing – review & editing, Funding acquisition.

Declaration of competing interest

The authors declare that they have no known competing financial interests or personal relationships that could have appeared to influence the work reported in this paper.

Acknowledgements

References

[1] J.W. Yeh, S.K. Chen, S.J. Lin, J.Y. Gan, T.S. Chin, T.T. Shun, C.H. Tsau, S.Y. Chang, Nanostructured high-entropy alloys with multiple principal elements: novel alloy design concepts and outcomes, Adv. Eng. Mater. 6 (2004) 299–303.

[2] B. Cantor, I.T.H. Chang, P. Knight, A.J.B. Vincent, Microstructural development in equiatomic multicomponent alloys, Mater. Sci. Eng. A 375–377 (2004) 213–218.

[3] Y. Zhang, T.T. Zuo, Z. Tang, M.C. Gao, K.A. Dahmen, P.K. Liaw, Z.P. Lu, Microstructures and properties of high-entropy alloys, Prog. Mater. Sci. 61 (2014) 1–93.

[4] Z.F. Lei, X.J. Liu, Y. Wu, H. Wang, S.H. Jiang, S.D. Wang, X.D. Hui, Y.D. Wu, B. Gault, P. Kontis, D. Raabe, L. Gu, Q.H. Zhang, H.W. Chen, H.T. Wang, J.B. Liu, K. An, Q.S. Zeng, T.G. Nieh, Z.P. Lu, Enhanced strength and ductility in a high-entropy alloy via ordered oxygen complexes, Nature 563 (2018) 546–550.

[5] Z.M. Li, K.G. Pradeep, Y. Deng, D. Raabe, C.C. Tasan, Metastable high-entropy dual-phase alloys overcome the strength-ductility trade-off, Nature 534 (2016) 227–230.

[6] B. Gludovatz, A. Hohenwarter, D. Catoor, E.H. Chang, E.P. George, R.O. Ritchie, A fracture-resistant high-entropy alloy for cryogenic applications, Science 345 (2014) 1153–1158.

[7] Q.Q. Ding, Y. Zhang, X. Chen, X.Q. Fu, D.K. Chen, S.J. Chen, L. Gu, F. Wei, H.B. Bei, Y.F. Gao, M.R. Wen, J.X. Li, Z. Zhang, T. Zhu, R.O. Ritchie, Q. Yu, Tuning element distribution, structure and properties by composition in high-entropy alloys, Nature 574 (2019) 223–227.

[8] T. Yang, Y.L. Zhao, Y. Tong, Z.B. Jiao, J. Wei, J.X. Cai, X.D. Han, D. Chen, A. Hu, J. J. Kai, K. Lu, Y. Liu, C.T. Liu, Multicomponent intermetallic nanoparticles and superb mechanical behaviors of complex alloys, Science 362 (2018) 933–937.

[9] Y.G. Yao, Z.N. Huang, P.F. Xie, S.D. Lacey, R.J. Jacob, H. Xie, F.J. Chen, A. Nie, T. C. Pu, M. Rehwoldt, D.W. Yu, M.R. Zachariah, C. Wang, R. Shahbazian-Yassar, J. Li, L.B. Hu, Carbothermal shock synthesis of high-entropy-alloy nanoparticles, Science 359 (2018) 1489–1494.

[10] W. Jiang, S.Y. Yuan, Y. Cao, Y. Zhang, Y.H. Zhao, Mechanical properties and deformation mechanisms of a Ni₂Co₁Fe₁V₀.₅Mo₀.₂ medium-entropy alloy at elevated temperatures, Acta Mater. 213 (2021) 116982.

[11] G. Laplanche, A. Kostka, O.M. Horst, G. Eggeler, E.P. George, Microstructure evolution and critical stress for twinning in the CrMnFeCoNi high-entropy alloy, Acta Mater. 118 (2016) 152–163.

[12] Y.Q. Wang, B. Liu, K. Yan, M.S. Wang, S. Kabra, Y.L. Chiu, D. Dye, P.D. Lee, Y. Liu, B. Cai, Probing deformation mechanisms of a FeCoCrNi high-entropy alloy at 293 and 77 K using in situ neutron diffraction, Acta Mater. 154 (2018) 79–89.

[13] S. Curtze, V.T. Kuokkala, Dependence of tensile deformation behavior of TWIP steels on stacking fault energy, temperature and strain rate, Acta Mater. 58 (2010) 5129–5141.

[14] S.S. Sohn, S. Hong, J. Lee, B.C. Suh, S.K. Kim, B.J. Lee, N.J. Kim, S. Lee, Effects of Mn and Al contents on cryogenic-temperature tensile and Charpy impact properties in four austenitic high-Mn steels, Acta Mater. 100 (2015) 39–52.

[15] Q.Y. Lin, J.P. Liu, X.H. An, H. Wang, Y. Zhang, X.Z. Liao, Cryogenic-deformation-induced phase transformation in an FeCoCrNi high-entropy alloy, Mater. Res. Lett. 6 (2018) 236–243.

[16] X.D. Xu, P. Liu, Z. Tang, A. Hirata, S.X. Song, T.G. Nieh, P.K. Liaw, C.T. Liu, M. W. Chen, Transmission electron microscopy characterization of dislocation structure in a face-centered cubic high-entropy alloy Al₀.₁CoCrFeNi, Acta Mater. 144 (2018) 107–115.

[17] F. Otto, A. Dlouhý, C. Somsen, H. Bei, G. Eggeler, E.P. George, The influences of temperature and microstructure on the tensile properties of a CoCrFeMnNi high-entropy alloy, Acta Mater. 61 (2013) 5743–5755.

[18] T.W. Zhang, S.G. Ma, D. Zhao, Y.C. Wu, Y. Zhang, Z.H. Wang, J.W. Qiao, Simultaneous enhancement of strength and ductility in a NiCoCrFe high-entropy alloy upon dynamic tension: micromechanism and constitutive modeling, Int. J. Plast. 124 (2020) 226–246.

[19] Y.T. Zhu, X.Z. Liao, X.L. Wu, Deformation twinning in nanocrystalline materials, Prog. Mater. Sci. 57 (2012) 1–62.

[20] J.P. Liu, X.X. Guo, Q.Y. Lin, Z.B. He, X.H. An, L.F. Li, P.K. Liaw, X.Z. Liao, L.P. Yu, J.P. Lin, L. Xie, J.L. Ren, Y. Zhang, Excellent ductility and serration feature of metastable CoCrFeNi high-entropy alloy at extremely low temperatures, Sci. China Mater. 62 (2019) 853–863.

[21] M. Naeem, H.Y. He, F. Zhang, H.L. Huang, S. Harjo, T. Kawasaki, B. Wang, S. Lan, Z.D. Wu, F. Wang, Y. Wu, Z.P. Lu, Z.W. Zhang, C.T. Liu, X.L. Wang, Cooperative deformation in high-entropy alloys at ultralow temperatures, Sci. Adv. 6 (2020) eaax4002.

[22] C. Zener, J.H. Hollomon, Effect of strain rate upon plastic flow of steel,, J. Appl. Phys. 15 (1944) 22–32.

[23] S.P. Tsai, Y.T. Tsai, Y.W. Chen, P.J. Chen, P.H. Chiu, C.Y. Chen, W.S. Lee, J.W. Yeh, J.R. Yang, High-entropy CoCrFeMnNi alloy subjected to high-strain-rate compressive deformation, Mater. Charact. 147 (2019) 193–198.

[24] L. Wang, J.W. Qiao, S.G. Ma, Z.M. Jiao, T.W. Zhang, G. Chen, D. Zhao, Y. Zhang, Z. H. Wang, Mechanical response and deformation behavior of Al₀.₆CoCrFeNi high-entropy alloys upon dynamic loading, Mater. Sci. Eng. A 727 (2018) 208–213.

[25] S.T. Zhao, Z.Z. Li, C.Y. Zhu, W. Yang, Z.R. Zhang, D.E.J. Armstrong, P.S. Grant, R. O. Ritchie, M.A. Meyers, Amorphization in extreme deformation of the CrMnFeCoNi high-entropy alloy, Sci. Adv. 7 (2021), eabb3108.

[26] X.Z. Gao, Y.P. Lu, J.Z. Liu, J. Wang, T.M. Wang, Y.H. Zhao, Extraordinary ductility and strain hardening of Cr₂₆Mn₂₀Fe₂₀Co₂₀Ni₁₄ TWIP high-entropy alloy by cooperative planar slipping and twinning, Materialia 8 (2019) 100485.

[27] M.J. Yao, K.G. Pradeep, C.C. Tasan, D. Raabe, A novel, single phase, non-equiatomic FeMnNiCoCr high-entropy alloy with exceptional phase stability and tensile ductility, Scripta Mater. 72–73 (2014) 5–8.

[28] Y. Deng, C.C. Tasan, K.G. Pradeep, H. Springer, A. Kostka, D. Raabe, Design of a twinning-induced plasticity high entropy alloy, Acta Mater. 94 (2015) 124–133.

[29] Z.G. Wu, Y.F. Gao, H.B. Bei, Thermal activation mechanisms and Labusch-type strengthening analysis for a family of high-entropy and equiatomic solid-solution alloys, Acta Mater. 120 (2016) 108–119.

[30] J.G. Li, T. Suo, C.X. Huang, Y.L. Li, H.T. Wang, J.B. Liu, Adiabatic shear localization in nanostructured face centered cubic metals under uniaxial compression, Mater. Des. 105 (2016) 262–267.

[31] W.W. Chen, B. Song, Split Hopkinson (Kolsky) Bar: Design, Testing, and Applications. Mechanical Engineering Series, Springer, New York, 2011.

[32] O. Dmitrieva, D. Ponge, G. Inden, J. Millán, P. Choi, J. Sietsma, D. Raabe, Chemical gradients across phase boundaries between martensite and austenite in steel studied by atom probe tomography and simulation, Acta Mater. 59 (2014) 364–374.

[33] D. Raabe, S. Sandlöbes, J. Millán, D. Ponge, H. Assadi, M. Herbig, P.P. Choi, Segregation engineering enables nanoscale martensite to austenite phase transformation at grain boundaries: a pathway to ductile martensite, Acta Mater. 61 (2013) 6132–6152.

[34] M. Kuzmina, D. Ponge, D. Raabe, Grain boundary segregation engineering and austenite reversion turn embrittlement into toughness: example of a 9 wt.% medium Mn steel, Acta Mater. 86 (2015) 182–192.

[35] W.S. Lee, C.F. Lin, Comparative study of the impact response and microstructure of 304L stainless steel with and without prestrain, Metall. Mater. Trans. 33 (2002) 2801–2810.

[36] W.S. Lee, C.F. Lin, T.H. Chen, H.W. Chen, Dynamic mechanical behaviour and dislocation substructure evolution of Inconel 718 over wide temperature range, Mater. Sci. Eng. A 528 (2011) 6279–6286.

[37] S. Fréchard, A. Redjaïmia, E. Lach, A. Lichtenberger, Dynamical behaviour and microstructural evolution of a nitrogen-alloyed austenitic stainless steel, Mater. Sci. Eng. A 480 (2008) 89–95.

[38] A. Rohatgi, K.S. Vecchio, G.T. Gray, The influence of stacking fault energy on the mechanical behavior of Cu and Cu-Al alloys: deformation twinning, work hardening, and dynamic recovery, Metall. Mater. Trans. 32 (2001) 135–145.

[39] A.A. Tiamiyu, A.G. Odeshi, J.A. Szpunar, Characterization of coarse and ultrafine-grained austenitic stainless steel subjected to dynamic impact load: XRD, SEM, TEM and EBSD analyses, Materialia 4 (2018) 81–98.

[40] A.A. Tiamiyu, A.G. Odeshi, J.A. Szpunar, Multiple strengthening sources and adiabatic shear banding during high strain-rate deformation of AISI 321 austenitic stainless steel: effects of grain size and strain rate, Mater. Sci. Eng. A 711 (2018) 233–249.

[41] H.L. Huang, Y. Wu, J.Y. He, H. Wang, X.J. Liu, K. An, W. Wu, Z.P. Lu, Phase-transformation ductilization of brittle high-entropy alloys via metastability engineering, Adv. Mater. 29 (2017) 1701678.

[42] T. Suo, Y.Z. Chen, Y.L. Li, C.X. Wang, X.L. Fan, Strain rate sensitivity and deformation kinetics of ECAPed aluminium over a wide range of strain rates, Mater. Sci. Eng. A 560 (2013) 545–551.

[43] Y.H. Zhao, J.F. Bingert, Y.T. Zhu, X.Z. Liao, R.Z. Valiev, Z. Horita, T.G. Langdon, Y. Z. Zhou, E.J. Lavernia, Tougher ultrafine grain Cu via high-angle grain boundaries and low dislocation density, Appl. Phys. Lett. 92 (2008) 081903.

[44] M.A. Meyers, Dynamic Behavior of Materials, John Wiley & Sons, New York, 1994.

[45] Y.F. Liu, Y. Cao, Q.Z. Mao, H. Zhou, Y.H. Zhao, W. Jiang, Y. Liu, J.T. Wang, Z. S. You, Y.T. Zhu, Critical microstructures and defects in heterostructured materials and their effects on mechanical properties, Acta Mater. 189 (2020) 129–144.

[46] W. Jiang, Y. Cao, Y.D. Jiang, Y.F. Liu, Q.Z. Mao, H. Zhou, X.Z. Liao, Y.H. Zhao, Effects of nanostructural hierarchy on the hardness and thermal stability of an austenitic stainless steel, J. Mater. Res. Technol. 12 (2021) 376–384.

[47] A.J. Zaddach, C. Niu, C.C. Koch, D.L. Irving, Mechanical properties and stacking fault energies of NiFeCrCoMn high-entropy alloy, JOM (J. Occup. Med.) 65 (2013) 1780–1789.

[48] W.S. Lee, C.Y. Liu, T.N. Sun, Deformation behavior of Inconel 690 super alloy evaluated by impact test, J. Mater. Process. Technol. 153–154 (2004) 219–225.

[49] J.G. Li, Y.L. Li, C.X. Huang, T. Suo, Q.M. Wei, On adiabatic shear localization in nanostructured face-centered cubic alloys with different stacking fault energies, Acta Mater. 141 (2017) 163–182.

[50] Z.Z. Li, S.T. Zhao, S.M. Alotaibi, Y. Liu, B.F. Wang, M.A. Meyers, Adiabatic shear localization in the CrMnFeCoNi high-entropy alloy, Acta Mater. 151 (2018) 424–431.

[51] J.M. Park, J. Moon, J.W. Bae, M.J. Jang, J. Park, S. Lee, H.S. Kim, Strain rate effects of dynamic compressive deformation on mechanical properties and microstructure of CoCrFeMnNi high-entropy alloy, Mater. Sci. Eng. A 719 (2018) 155–163.

[52] F. Dalla Torre, P. Spätig, R. Schäublin, M. Victoria, Deformation behaviour and microstructure of nanocrystalline electrodeposited and high pressure torsioned nickel, Acta Mater. 53 (2005) 2337–2349.

[53] R.P. Carreker, W.R. Hibbard, Tensile deformation of high-purity copper as a function of temperature, strain rate, and grain size, Acta Metall. 1 (1953) 654–663.

[54] N. Kumar, Q. Ying, X. Nie, R.S. Mishra, Z. Tang, P.K. Liaw, R.E. Brennan, K. J. Doherty, K.C. Cho, High strain-rate compressive deformation behavior of the Al$_{0.1}$CrFeCoNi high entropy alloy, Mater. Des. 86 (2015) 598–602.

[55] P.S. Follansbee, U.F. Kocks, A constitutive description of the deformation of copper based on the use of the mechanical threshold stress as an internal state variable, Acta Metall. 36 (1988) 81–93.

[56] M.Z. Butt, P. Feltham, Work hardening of polycrystalline copper and alpha brasses, Met. Sci. 18 (1984) 123–126.

[57] S.I. Hong, J. Moon, S.K. Hong, H.S. Kim, Thermally activated deformation and the rate controlling mechanism in CoCrFeMnNi high entropy alloy, Mater. Sci. Eng. A 682 (2017) 569–576.

[58] M.J. Jang, S.H. Joo, C.W. Tsai, J.W. Yeh, H.S. Kim, Compressive deformation behavior of CrMnFeCoNi high-entropy alloy, Met. Mater. Int. 22 (2016) 982–986.

[59] R.P. Zhang, S.T. Zhao, J. Ding, Y. Chong, T. Jia, C. Ophus, M. Asta, R.O. Ritchie, A. M. Minor, Short-range order and its impact on the CrCoNi medium-entropy alloy, Nature 581 (2020) 283–287.

[60] Z.J. Zhang, M.M. Mao, J.W. Wang, B. Gludovatz, Z. Zhang, S.X. Mao, E.P. George, Q. Yu, R.O. Ritchie, Nanoscale origins of the damage tolerance of the high-entropy alloy CrMnFeCoNi, Nat. Commun. 6 (2015) 10143.

[61] H. Mecking, U.F. Kocks, Kinetics of flow and strain-hardening, Acta Metall. 29 (1981) 1865–1875.

[62] U.F. Kocks, H. Mecking, Physics and phenomenology of strain hardening: the FCC case, Prog. Mater. Sci. 48 (2003) 171–273.

[63] P.M. Anderson, J.P. Hirth, J. Lothe, Theory of Dislocations, third ed., Cambrige University Press, Cambrige, 2017.

[64] S. Amelinckx, Dislocations in particular structures, in: F.R.N. Nabarro (Ed.), Dislocations in Solids, vol. 2, North-Holland, Amsterdam, 1979, p. 146.

[65] K. Rajan, Stacking fault strengthening in low stacking fault energy alloys, Scripta Metall. 17 (1983) 101–104.

[66] J. Yoo, K. Choi, A. Zargaran, N.J. Kim, Effect of stacking faults on the ductility of Fe-18Mn-1.5Al-0.6C twinning-induced plasticity steel at low temperatures, Scripta Mater. 137 (2017) 18–21.

[67] W. Püschl, Models for dislocation cross-slip in close-packed crystal structures: a critical review, Prog. Mater. Sci. 47 (2002) 415–461.

[68] O. Bouaziz, S. Allain, C. Scott, Effect of grain and twin boundaries on the hardening mechanisms of twinning-induced plasticity steels, Scripta Mater. 58 (2008) 484–487.